Computers in Biology and Medicine 43 (2013) 1353–1362

Contents lists available at ScienceDirect

Computers in Biology and Medicine

journal homepage: www.elsevier.com/locate/cbm

Image-based computational hemodynamics evaluation of atherosclerotic carotid bifurcation models

Jingliang Dong, Kiao Inthavong, Jiyuan Tu*

School of Aerospace, Mechanical & Manufacturing Engineering, and Health Innovations Research Institute (HIRi), RMIT University, PO Box 71, Bundoora, VIC 3083, Australia

ARTICLE INFO

Article history:
Received 7 May 2013
Accepted 19 June 2013

Keywords:
Computational hemodynamics
Atherosclerotic carotid bifurcation
Wall shear stress
Pressure drop coefficient
Time duration

ABSTRACT

Widely accepted treatment for carotid artery stenosis includes stenting as well as carotid endarterectomy (CEA), despite complications associated with distal embolism. Therefore pre-screening for evaluating the extent of a stenosis is critically important before undertaking surgical procedures. This study presents and evaluates the feasibility of implementing a virtual computational hemodynamics platform for clinical use to determine the severity of a stenosis and give guidance for surgical decision making. The virtual platform incorporates high-resolution three-dimensional angiography results with Computational Fluid Dynamics modeling to determine clinically related indicators. This includes wall shear stress (WSS), the spatial and temporal hemodynamic changes of blood flow within patient-specific carotid bifurcations, pressure drop coefficient, and severity stratification. The turn-around time for each computational modeling stage was examined which showed that the total time cost is practical and the proposed hemodynamics evaluation platform is reasonably efficient for clinical diagnosis. Furthermore the virtual platform may be used to detect the hemodynamic consequence of atherogenesis, which can then be addressed and quantified based on the distribution of WSS related flow indicators on the abnormal luminal fractions. Additional functional evidence and data can be used by the overseeing physician to enrich and complement the anatomical information for more in-depth evaluation of stenosis in a reasonable time duration.

1. Introduction

Atherosclerosis is a chronic disease of artery vessels whereby the artery walls thicken causing the lumen size for blood transport to narrow. It is reported that 80% of all strokes that occur annually in the western world are ischemic and around 30% of these are due to thromboemboli arising from atherosclerotic lesions at the carotid artery bifurcation [1]. As atherosclerosis can remain asymptomatic for decades [2], accurate prevalence and incidence rates of carotid artery stenosis (CAS) are difficult to ascertain. Therefore, the consequence of CAS can be easily underestimated as many patients do not seek medical attention despite having CS for a prolonged period.

The diagnosis of symptomatic CAS relies on a combination of history, clinical examination and imaging derived from CT, MR imaging, ultrasonographic and angiographic images. The evaluation of angiographic images is limited to the geometric measurement determining the degree of stenosis, leaving the ultimate stenosis evaluation to the experience of the treating physician. For symptomatic patients who undertake carotid endarterectomy, the risk of fatal stroke to a severe CAS is reduced to 13% over 2 years [3]. The report by the ECST Group [3] concluded that while a strong correlation exists between severe CAS and stroke incidence, using anatomical stenosis geometry as a single indicator of risk of stroke is poorly justified. In addition, even a thorough clinical history record can further assist the physician to assess stroke risk. Due to the wide range of treatment options, a reliable way has to be found to select the most appropriate option for each patient.

Taxon [4] has shown that frequent occurrence of localized atherosclerotic plaques in curvature, bifurcation, and branching of arterial vessel regions suggest that fluid dynamics and vessel geometry may have an influence in plaque formation. Computational fluid dynamic (CFD) methods can offer additional functional information from a hemodynamics point of view to complement the vessel geometry information, detailed *in-vivo* angiographic imaging or *in-vitro* experimental velocimetry measurements.

Many numerical hemodynamic studies have been performed to investigate the hemodynamic influence on CAS progression, which has established that the magnitude and gradient of blood flow near the vessel wall, or the wall shear stress, is a source of pathogenesis of CAS [5–7]. Vessels exposed to low wall shear

* Corresponding author. Tel.: +61 3 9925 6191; fax: +61 3 9925 6108.
E-mail address: jiyuan.tu@rmit.edu.au (J. Tu).

0010-4825/$ - see front matter © 2013 Elsevier Ltd. All rights reserved.
http://dx.doi.org/10.1016/j.compbiomed.2013.06.013

stress appear to be more prone to plaque development based on an MR imaging based study using 21 carotid arteries [6]. Researchers determined that the investigations of local risk indicators such as time-averaged wall shear stress (TAWSS) and oscillatory shear index (OSI) in atherosclerosis did not rely on all the surrogate geometric markers of disturbed flow [7]. While atherosclerotic disease is a multifactorial disease, hemodynamic forces and wall shear stress mapping can provide a complementary determinant among a multidisciplinary approach for early atherosclerosis detection. Therefore obtaining such data must be prompt in order for it to be of clinical use.

Although numerous studies of carotid artery bifurcations have been performed, most have concentrated on analyzing the blood flow pattern within the stenotic district through various modeling assumptions, such as steady flow [8], pulsatile flow [9], rigid vessel [10], compliant vessel [11], Newtonian flow [12], non-Newtonian flow [13,14], and anatomical effects, including artery branching [15], bifurcation angles [13,16] and wall curvature [17]. LaDisa et al. [18] have numerically examined the influence of WSS and OSI in progression of plaques in a clinically reasonable time-frame. However, the hemodynamic burden (effect on blood flow transportation) caused by the existence of the plaque was not investigated, which is an important practical indicator in helping the treating physician for carrying out risk stratification and arranging appropriate treatments.

In order to reveal the stenotic lesion burden and its influence exerting on the blood flow transport in an efficient time, as many assumptions as possible should be accounted for while omitting those that are less relevant and are time consuming. This will allow an efficient CFD based diagnosis assistance platform for atherosclerotic carotid bifurcation treatment as a step towards improving surgical planning and therapy outcomes. In this paper, a robust and time-efficient computational hemodynamics platform is proposed, and clinical related indicators are introduced for data processing and severity stratification of CAS. Ten carotid artery bifurcations were reconstructed from MR scans, and intravascular flow patterns were predicted using CFD analysis with a fine structured mesh and a non-Newtonian viscosity model. The stenosis-induced flow performance and the flow disturbance in pre-stenosis and post-stenotic regions were examined and this was integrated with high resolution anatomical measurements for direct and long-term plaque burden evaluation. Each step in the work flow was monitored for reproducing reasonable results with a minimized time cost. This proposed framework is a step towards an e-health platform that can assist both doctors and patients to have a better understanding of CAS disease and to provide better guidance for clinical treatment.

2. Methodology

Patient-specific realistic carotid bifurcation models were reconstructed from MR image data and their corresponding stenosis severity were anatomically assessed. Then, a computational hemodynamics approach was proposed and performed on these patient-specific carotid bifurcation models. Prior to that, the numerical accuracy of the proposed modeling approach was evaluated through comparison of numerical and experimental results on the basis of two standard idealized carotid bifurcation models. Finally, the hemodynamics performance and computational efficiency were examined for clinical diagnostic purposes.

2.1. MR imaging

High resolution MR imaging of carotid bifurcations was performed on patients using a 1.5 T General Electric scanner. All human experiments were approved by the Monash Medical Center and an Institutional Review Board. The MR imaging was first performed on four patients, which constitute a total of eight models that pertain to their left and right carotid bifurcations. Then another two additional carotid bifurcation models were scanned from two additional patients of which only one artery from each pair of carotid arteries were selected. Altogether, ten patient-specific models were imaged from six patients. For each carotid artery, a total of 112 contiguous slices were generated from the high-resolution T-1 weighted spoiled gradient echo with parameters as follows: TR, 35 ms; TE, 7 ms; flip angle, 35°; field of view, 24 cm; voxel size 0.63 mm × 0.73 mm × 0.63 mm.

2.2. Arterial model reconstruction

Based on the MR imaging data, the computational model was reconstructed using a commercial software Mimics (Materialise HQ, Belgium). The specific structures of interest were extracted out based on a thresholding range of gray scale values in the segmentation process. This approach separates the luminal area from the rest of the tissues. Though this is a simple technique, there remain factors that can complicate the thresholding operation. For example, non-stationary and correlated noise, ambient illumination, busyness of gray levels within the object and its background, inadequate contrast, and object size not commensurate with the scene. All these factors require considerable manual operation during the segmentation process. A 3D model is then exported as a '.stl' (stereolithography) file. Fig. 1 shows the ten patient-specific carotid artery models that were produced. The common carotid artery (CCA), internal carotid artery (ICA) and external carotid artery (ECA) are labeled for each model. In addition to these patient specific models, two standard geometry models are created. These standard idealized stenotic model are the 63% ICA stenosis averaged tuning-fork shaped human carotid bifurcation (ST-AHCB) model, and the plain tuning-fork shaped human carotid bifurcation (TF-ACHB) [19]. These models will be used as a benchmark model for comparisons, as it is well-defined and has been used extensively in the literature. A schematic diagram of these two idealized carotid bifurcation models is illustrated by Fig. 2, and their detailed dimensions are given in Table 1.

2.3. Anatomical assessment

Anatomical measurements to obtain two characteristic parameters, stenosis diameter *A* and distal diameter *B* were performed on each model and the values presented in Table 2. A schematic diagram of an artery stenotic region is shown in Fig. 3 to highlight the characteristic parameters.

In clinical trials, one way to estimate the degree of carotid stenosis is to calculate distal diameter reduction (DDR) through comparing the diameter of the residual lumen at the site of the stenosis (variable *A* in Table 2) to the diameter of the distal unaffected lumen (variable *B* in Table 2) [20], and the degree of stenosis for the studied carotid models examined by DDR method are shown in Table 2. It is found that nine models were experiencing one or two sites of stenosis except model 9, which exhibited no significant diameter variation in its radial direction. In terms of pathological location, six models (models 2 and 4–8) suffered stenotic lesions on the ICA; two models (models 1 and 10) presented stenotic lesions on both ICA and ECA, while only one model (model 3) had a CCA stenosis. In terms of stenosis severity, four carotid models (models 1–3 and 6) experienced larger than 50% DDR in their stenosis lesions, and model 2 was suffering a DDR of 71.58% at its ICA branch, which is the most severe case among all models.

However, the generated anatomical information does not represent a dynamic stenosis burden under transient blood flow, and a further analysis of stenosis-induced influence on arterial blood flow transportation will be much more functional in clinical

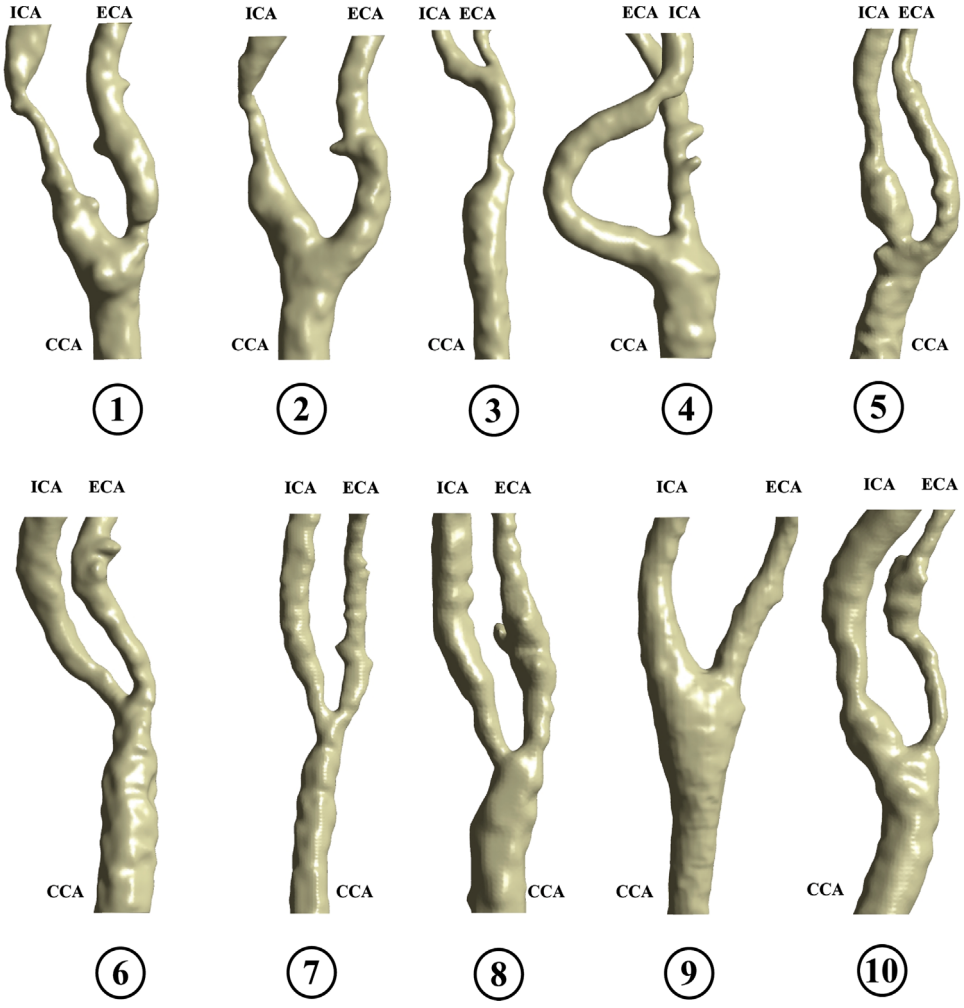

Fig. 1. Reconstructed patient-specific carotid artery models.

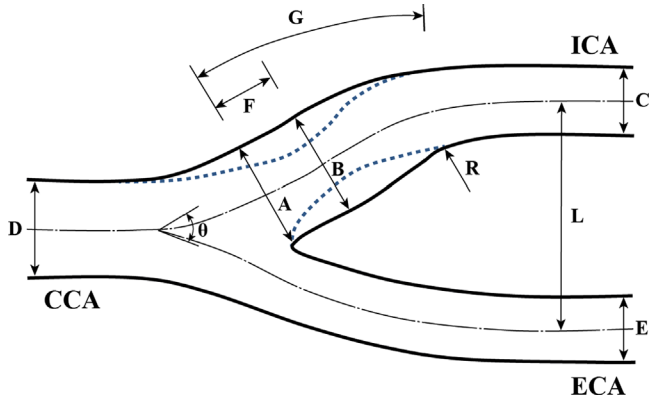

Fig. 2. Schematic representation of the carotid artery models: solid line represents the healthy TF-AHCB model, and the dashed line represents the 63% ICA stenosed ST-AHCB model.

Table 1
Dimensions of the idealized carotid bifurcation models.

Indicated locations	D	A	B	C	E	F	G	L	R
Dimensionless values	1.0	1.04	1.11	0.72	0.69	0.9	3.0	2.4	4.1
TF-AHCB	20	20.8	22.2	14.4	13.8	18.0	60	48	82
ST-AHCB	20	16.8	8.8	14.4	13.8	18.0	60	48	82

Dimensions in (mm), $\theta = 50^{\circ}$ for all models.

applications. Therefore, a computational hemodynamics approach is needed to investigate the stenosis effects on intravascular blood flow patterns and blood transportation performances.

2.4. Computational mesh generation for CFD

The carotid bifurcation CFD models were generated with a structured hexahedral mesh using a multi-block O-grid method within ICEM CFD (ANSYS, US). A structured mesh reduces numerical diffusion and requires lower cell counts than unstructured meshes. A near wall grid refinement was imposed on each model to provide better resolution for near wall quantities, such as WSS. A representative diagram of meshing process is shown in Fig. 4, based on a 63% ICA stenosis ST-AHCB model [19]. Due to the complexity and diversity of patient-specific models, customized multi-block topology was needed to fit the rapid vessel geometrical variation and all the regions with high curvature or stenosis into refined blocks, which requires additional time costs.

2.5. Boundary conditions and fluid property modeling

2.5.1. Inlet boundary condition

As the inlet flow waveforms corresponding to each model were unavailable since the patient could not be re-traced, a representative ensemble flow waveform from 17 healthy models reported by

Table 2
Anatomical measurements of studied patient-specific carotid artery models.

ID	Stenosis location		Stenosis diameter A (mm)	Distal diameter B (mm)	Distal diameter reduction (DDR) $(1-A/B)\times 100\%$	Stenotic surface area $S_{Diseased}$ (mm^2)	Total surface area S_{Total} (mm^2)
1	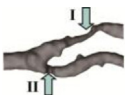	**I**	1.88	5.64	66.67%	138.11	1299.11
		II	2.65	4.41	39.91%	61.06	
2		**I**	1.58	5.56	71.58%	132.02	1144.76
3		**I**	1.92	4.07	52.83%	79.89	879.86
4	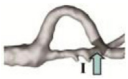	**I**	2.73	3.64	25.00%	56.41	1231.04
5	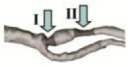	**I**	3.73	5.89	36.67%	67.41	1189.25
		II	2.57	3.75	31.47%	72.58	
6	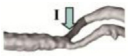	**I**	2.56	5.70	55.09%	119.29	1381.07
7	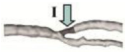	**I**	2.82	3.98	29.15%	72.80	1405.45
8		**I**	2.74	4.25	35.53%	88.19	1005.20
9		–	–	–	–	–	1620.42
10	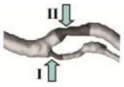	**I**	1.75	2.19	20.09%	38.57	1211.42
		II	2.99	4.85	38.35%	180.35	

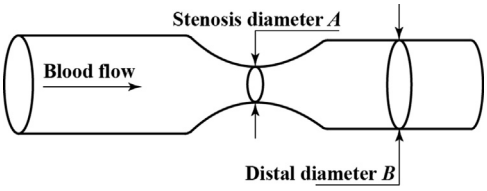

Fig. 3. Simplified schematic diagram of artery stenotic region.

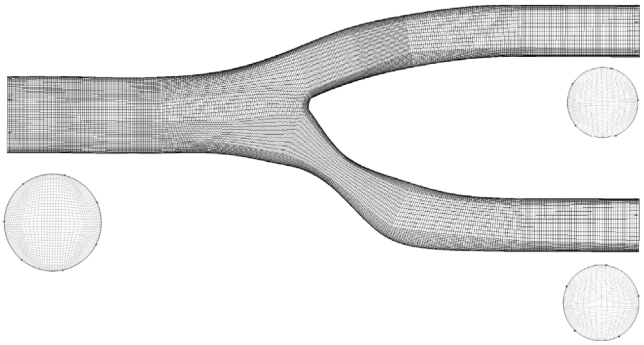

Fig. 4. Structured mesh result of the 63% ICA stenosed ST-AHCB model.

Holdsworth et al. [21] is adopted (Fig. 5). This boundary condition is imposed on the inlet of each model using a temporally varying Womersley velocity profile. This type of velocity profile describes the characteristic of oscillatory flow (presumed to be laminar and incompressible) in a tube arising in the solution of the linearized Navier–Stokes equations. The analytical solution to this problem is given by Zamir [22] in the following form:

$$u_1(r,t)=\frac{k_s}{4\mu}(r^2-a^2)+\frac{ik_sa^2}{\mu a^2}\left(1-\frac{J_0(\varsigma)}{J_0(\Lambda)}\right)e^{iwt}, \quad (1)$$

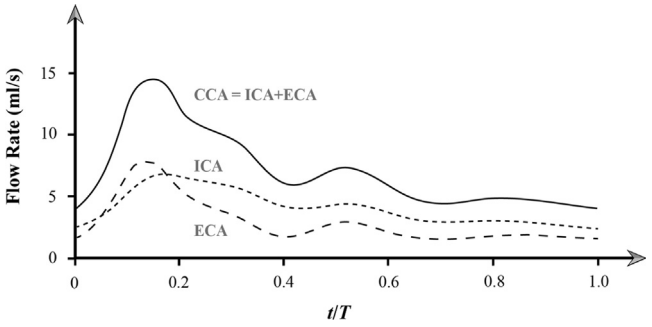

Fig. 5. Volume flow rates of a healthy carotid model.

where t is time; r is the radial coordinate; a is the radius of artery; k_s is the steady-state part of the pressure gradient; J_0 is the Bessel function of order zero of the first kind; ω are angular frequencies after Fourier Transformation; and $\Lambda=i^{3/2}\alpha$ is the complex frequency parameter. For flows with low frequency (1 or less), the solution can be further simplified using a series expansion of the Bessel function:

$$u_1(r,t)\approx\frac{k_s}{4\mu}(r^2-a^2)(1+\cos\omega t). \quad (2)$$

This means the frequency of pulsations is sufficiently low and that a parabolic velocity profile has sufficient time to develop during each cycle. The flow becomes nearly in phase with the pressure gradient, and the relation between flow and pressure can be treated instantaneously the same as in the case of a steady Poiseuille flow.

2.5.2. Outlet boundary conditions

The downstream peripheral vascular impedance (DPVI) model was adopted for the outlet boundary. The main purpose of this method is establishing a feasible and efficient hemodynamics

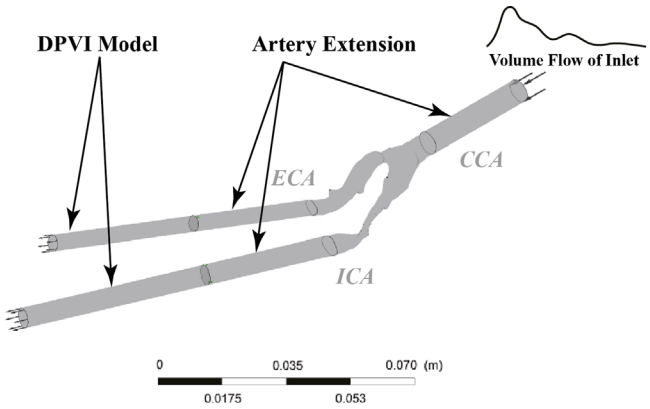

Fig. 6. A schematic diagram of the DPVI modeling method.

framework through connecting two porous domains with different transient permeability configurations to outlets of truncated carotid bifurcation models (Fig. 6). This method has been implemented in a previous paper and additional details can be obtained in [23].

2.5.3. Fluid transport property model

The shear thinning and viscoelasticity of blood are closely relevant to its microscopic structures, such as aggregation, deformation and alignment of the red blood cells, where the red blood cells mainly determine the rheological behavior of blood. However, Gijsen et al. [8,24] have demonstrated that viscoelasticity can be ignored for the prediction of velocity since the shear thinning behavior dominates the non-Newtonian property of the blood flow. In this study, the shear thinning behavior is governed by the Carreau–Yasuda model [25], and the relationship between blood viscosity η and shear rate γ is

$$\frac{\eta-\eta_\infty}{\eta_0-\eta}=[1+(\lambda\gamma)^a]^{(n-1)/a}, \tag{3}$$

where η_∞ is the viscosity for an infinite shear rate, and η_0 is the plasma viscosity at zero shear rate. λ, n, and a are fitting parameters, which are borrowed from the experimental data based on a well-tested blood-mimicking fluid [8,24]. These parameters have the following values: $\eta_\infty=3.7\times10^{-3}$ Pa s, $\eta_0=3.14\times10^{-2}$ Pa s, $\lambda=2.517$ s, $n=0.5736$, $a=2$, and $\rho=1060$ kg m^{-3}.

2.6. CFD simulation

Each computational mesh was imported into ANSYS CFX, which uses a finite volume method to solve the unsteady incompressible Navier–Stokes equations. The discretization used a second order implicit backward Euler method. Grid independence was performed which found that the mesh element character length was set as 0.4 mm and the choice of transient simulation time step was fixed at 0.005 s referred from [23]. Vessel walls were assumed to be rigid for all simulations [26]; the convergence criterion for the relative residual of all dependent variables was set as 1×10^{-4} for each time step. For the simulation, two full cardiac cycles were required to damp out the initial transient errors. Therefore, a total of three full cardiac cycle calculations were performed with the last cycle used for data analysis [27].

2.7. Turbulence modeling

In general, the blood flow in large arteries can be treated as laminar if all vessels are typically normal and healthy in geometry without any significant constrictions. However, where atherosclerosis is present in arteries, these regions of severe constrictions will experience a vastly different biomechanical environment that exhibits the presence of transitional and turbulent flow in comparison with healthy vessels [28]. The WSS within the stenotic region is usually high because the area reduction accelerates the blood flow within the stenosis, while in the post-stenotic region, low oscillatory WSS is formed due to the existence of flow separation and an oscillatory vortex. The high WSS and the presence of turbulence may damage the endothelial cells [29,30], which can induce plaque rupture and generate thrombosis [31,32]. In addition, high temporal shear gradients are also shown to stimulate endothelial cell proliferation [33].

During past decades, many *in-vitro* measurements [34,35] and numerical studies using turbulence models [36,37] were performed on stenotic arterial vessels, which have provided visualization of the flow characteristics in proximal and post-stenotic regions. The flow is significantly influenced by the vessel geometry and is far from being laminar in character. In order to capture various types of transition mechanisms and to evaluate the numerical accuracy against comparable experiment, the 'transitional SST model' developed by Menter et al. [38] is used. This model is based on two additional transport equations to solve the turbulence kinetic energy k and the specific dissipation ω: the first is an intermittency equation (γ-equation), used to trigger the transition process; and the second is the transition onset momentum thickness Reynolds number equation ($Re_{\theta t}$-equation), which is forced to follow experimentally-determined correlations. The model uses a new empirical correlation to cover standard bypass transition as well as flows in low free-stream turbulence environments.

Prior to carrying out the patient-specific carotid bifurcation analysis, numerical simulations based on an healthy averaged human tuning-fork shaped idealized carotid bifurcation (TF-AHCB) model and a ST-AHCB model having ICA sinus with an 63% axi-symmetric cross-sectional area reduction were performed and the results were compared with a published particle image velocimetry (PIV) work using the same geometries [19,39]. Both the experimental and numerical studies used a steady flow rate at Re=400 and Re=800, which are representative of the mean and peak systolic flow conditions. The working liquid was an aqueous glycerin solution (61% by weight), with dynamic viscosity of 11.7×10^{-3} Pa s, and density of 1150 kg m^{-3} at 20 °C [39].

3. Results and discussion

3.1. CFD model validation

Fig. 7 presents the comparison between numerically predicted and PIV measurements from Buchmann et al. [19,39] of the stream-wise flow patterns at the center-plane of a healthy and stenotic idealized carotid artery models. All the velocities were normalized with the maximum value at the centerline of the CCA inlet. In order to simplify outlets conditions, rather than adopting DPVI model mentioned before, all simulations and measurements in this section, the flow division ratio between ICA and ECA (Q_{ICA}/Q_{ECA}) was set as 7/3 according to Ku et al. [40]. For the TF-AHCB model, due to its healthy vessel shape, the blood flow remains laminar, thus laminar flow modeling is used. However, for the ST-AHCB model, as it is highly stenosed at the ICA sinus, the transitional-SST model is used to predict the transitional flow patterns occurring proximal and downstream of the stenotic region.

In general, the predicted stream-wise flow patterns are in satisfactory agreement with the measured data. Compared with the PIV data, flow separation and recirculation regions due to the abrupt cross-sectional area expansion at the ICA sinus region of the TF-AHCB model are successfully predicted by the numerical simulation based on a laminar model (Fig. 7a). For the ST-AHCB model (Fig. 7b), the velocities predicted at the stenotic site (using the transitional turbulence model)

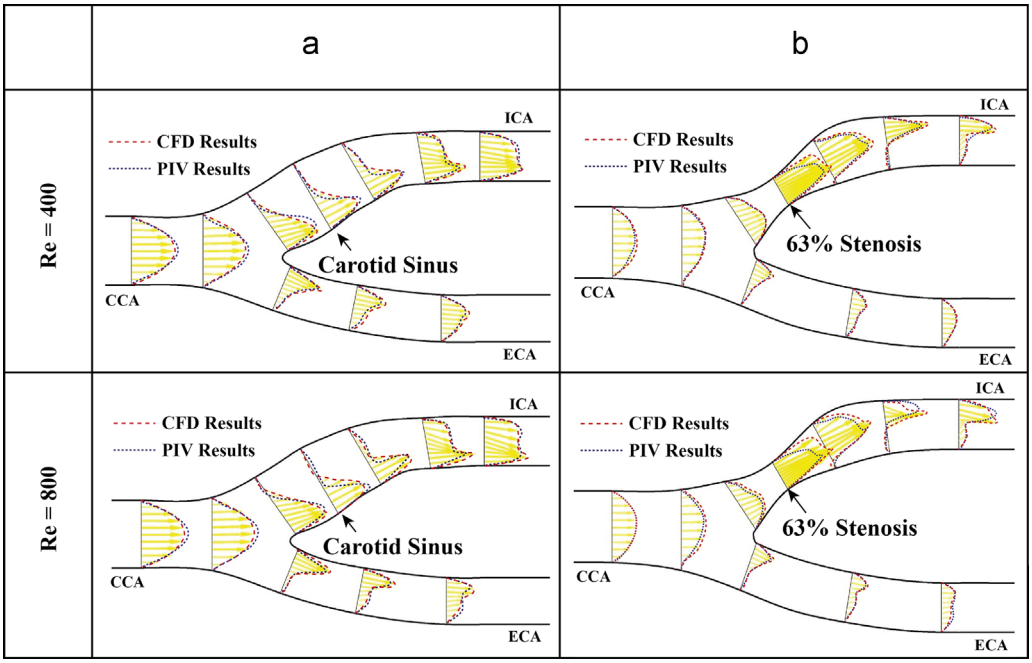

Fig. 7. Comparison between numerical and referred PIV experimental results based on TF-AHCB model and ST-AHCB model.

were over-predicted for both Reynolds number conditions, where the maximum differences are 16.2% for Re=400 and 27.8% for Re=800, but for the other regions of this model, a good agreement with the experimental data was found. Nonetheless, this order of error is comparable to published works, which has reported maximum relative errors between numerical and experimental results of 40% [41] and 55% [42], respectively. The better prediction performance in this paper may be due to the steady flow condition and the use of a transitional turbulence model. The ST-AHCB model was also simulated using a laminar model which produced slightly worse comparisons with the experimental data. Therefore, the basic numerical configurations used in this paper are capable of providing more accurate information of the intravascular flow field for both healthy and stenotic carotid bifurcation models.

3.2. Hemodynamics assessment with WSS based parameters

Two widely adopted flow indicators TAWSS (time-averaged wall shear stress) and OSI (oscillatory shear index) are used to evaluate the total shear stress exerted on the wall throughout a cardiac cycle [23]. In particular, the OSI can be regarded as the fraction of angle and magnitude change between the instantaneous WSS and the time-averaged WSS. It ranges from 0 to 0.5, where 0 represents a unidirectional WSS and the theoretical maximum value (0.5) describes a purely unsteady, oscillatory flow with zero WSS. Areas of high OSI are predisposed to endothelial dysfunction and atherogenesis [40,43], while abnormally high TAWSS (higher than 40 Pa) values can cause direct endothelial injury and increase the risk of getting thrombosis [44].

An example of the CFD simulation (as an animation) showing the geometry and one cardiac cycle that highlights the WSS variation for a representative stenotic model (model 2) is given in the online supplementary data. The TAWSS during one cardiac cycle was quantified and is shown in Fig. 8. It is found that high WSS is concentrated at the stenosis regions and all the stenotic models experienced abnormally high WSS (larger than 40 Pa) at their lesion sites, which may lead to fissuring and affect macrophage distribution leading to plaque destabilization and rupture [45]. The OSI distribution for each case is shown in Fig. 9, where most of the high OSI regions (highlighted by boxes with solid lines) are found at the bifurcation bulge (model ID 1, 2, 4, 9). This confirms that the bifurcation is one of the most susceptible sites to experience disturbed flow and low unhealthy shear stress, which can lead to endothelial dysfunction and atherogensis [46] while the other susceptible anatomical locations are curved regions in the branches.

Supplementary material related to this article can be found online at http://dx.doi.org/10.1016/j.compbiomed.2013.06.013.

As a developing atherosclerotic lesion can itself alter the local blood flow patterns after a substantial stenosis is formed, an elevated velocity of blood flow through the narrowed luminal space can lead to flow separation (disturbed flow which can be quantified by OSI) occurring immediately downstream of the stenosis. These disturbed flow regions induced by stenotic lesions are highlighted by boxes with dashed lines in Fig. 9. The disturbed flow regions impose similar implications to the downstream endothelial cells as seen in the carotid bifurcation bulge, but at a reduced scale (model ID 1, 3, 6, 7, 8, 10). Eventually, the lesion-induced flow disturbances may contribute to a continuous streamwise growth of the lesion over time, as many studies of endothelial cells have demonstrated that such a hemodynamic environment promotes pro-inflammatory gene and protein expression which is conducive to increased atherosclerosis susceptibility [47].

Further assessment of the lesion burden on the carotid bifurcation is analyzed by determining the luminal surface area that experiences high WSS (larger than 40 Pa), given as S_{HWSS}, and the proportion of the high WSS affected area over the total carotid surface area given as P_{HWSS} and is shown in Fig. 10. Models 1–3 suffered larger regions of high WSS compared with models 4–8 and 10. Models 1, 2, and 3 exhibited 77.54 mm^2, 94.87 mm^2 and 33.05 mm^2 luminal surface area respectively, where high risk of direct endothelial injury and plaque erosion exists due to the abnormally high wall shear. In addition, the variation of P_{HWSS} presented a similar trend as S_{HWSS} distribution. Models 1, 2, 3 also exhibited a greater high WSS load (5.80%, 8.08% and 3.03%, respectively) when compared with the rest of the stenotic carotid models.

3.3. Hemodynamics assessment with clinical trials used indicators

Pressure probe wire based fractional flow reserve (FFR) is widely used to evaluate the physiological significance of the stenosis [48,49].

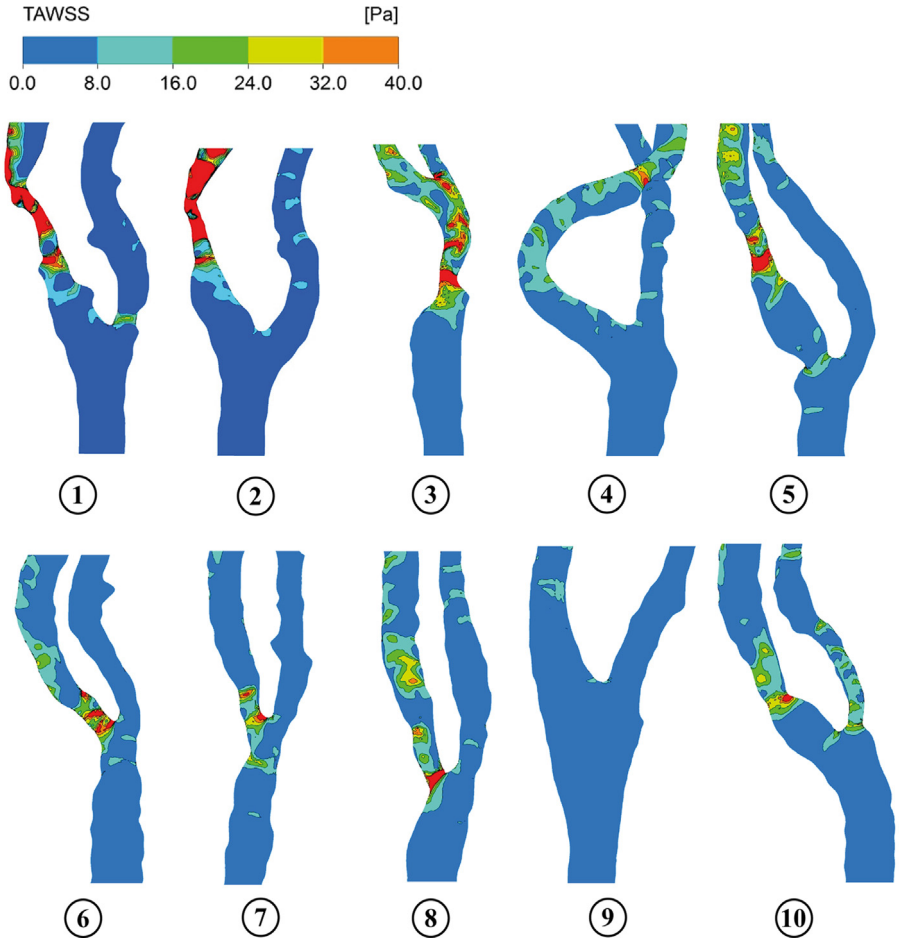

Fig. 8. Time-averaged WSS distributions of the ten studied carotid bifurcation models.

For a stenotic artery as shown by Fig. 3, the FFR is defined as the ratio of maximum blood flow in a stenotic artery to the normal maximum flow in the same vessel. It can be determined by the mean pressure value taken distal to the stenosis compared with the mean proximal pressure at peak vasodilation. Therefore, the FFR has a lower and upper limits of 0 and 1, which represent complete vessel occlusion, and no obstruction, respectively. For diagnosis of coronary artery stenosis, if the FFR value is less than 0.75, angioplasty of the diseased artery vessel is recommended [50,51]. However, the presence of a physical probe wire also reduces the intravascular flow and alters the pressure drop, which in turn leads to false FFR values [52]. This can impede on the decision making for the clinicians in the assessment of a stenosis. The current CFD simulation can be a useful technique to overcome this drawback and enable clinicians to carry out better analysis over different clinical situations, instead of complicated *in-vivo* measurements.

In this paper, one pressure drop based diagnostic parameter, pressure drop coefficient (CDP_e), developed by Banerjee et al. [53] is introduced for stenosis severity stratification. The CDP_e is defined as the ratio of mean trans-stenotic pressure drop, $\Delta\tilde{p}$, (superscript '~' indicates temporal average quantity) to the proximal dynamic pressure and is give as

$$CDP_e = \frac{\Delta\tilde{p}}{0.5\rho\tilde{\tilde{u}}_e^2}, \tag{4}$$

where ρ is blood density, $\tilde{\tilde{u}}_e$ is spatial and temporal mean blood flow velocity in the proximal vessel.

The FFR–CDP_e correlation is depicted in Fig. 11, and this linear relation is obtained from a three points' strains statistical reasoning. This linear relation can be written into the following equation as:

$$CDP_e = -1015.8\ FFR + 923.26 \tag{5}$$

Unlike FFR, CDP_e is not limited between small range. In detail, the variation range of FFR is 0.6–0.9, where the corresponding value range of CDP_e is 0–300. Therefore, a larger and more accurate threshold value can be established for CDP_e in human clinical trials. According to the threshold of FFR in clinical applications [50], if the CDP_e value is larger than 161.41, proper vascular interventions should be recommended.

The CDP_e values for all the nine stenotic carotid models were calculated and shown in Table 3. Their corresponding FFR values were also examined based on Eq. (5). It should be noted that the CDP_e values in Table 3 only included the most severe lesion value if the studied carotid bifurcation model suffered a multi-site stenosis. It can be found that only one carotid artery (model 2) experienced an abnormally high CDP_e value 235.67, which exceeds the prescribed threshold 161.41 for 46%, therefore the maximum blood flow in this stenotic branch can only account for 67.69% of its normal situation. This result also confirms with the anatomical assessment conclusion that model 2 was suffering the most severe stenosis degree (71.58% of DDR) among all carotid models. In contrast, the pressure drop coefficients for the other 8 stenotic models were much lower than 161.41, hence the occlusion effect on the blood flow transportation due to the present of the stenosis lesions was less than 20%.

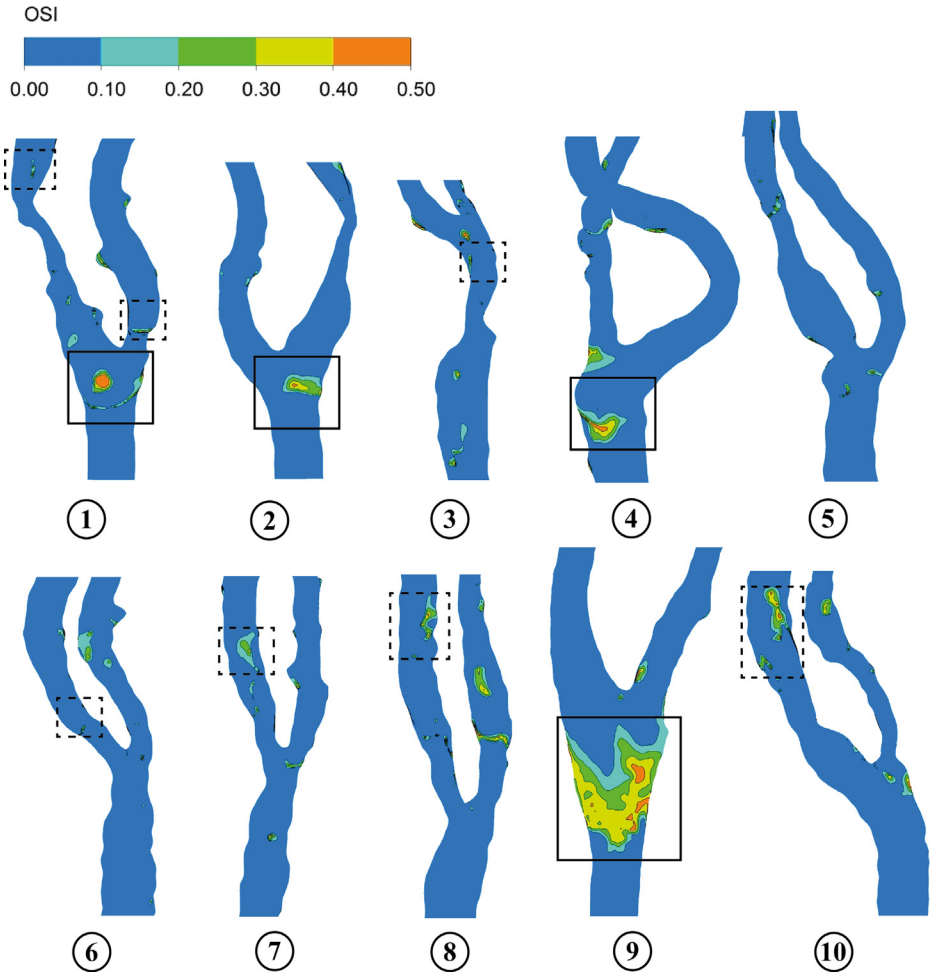

Fig. 9. OSI distributions of the ten studied carotid bifurcation models. Boxes with a solid line indicate high OSI regions, while boxes with dashed lines indicate disturbed flow induced by stenotic lesions.

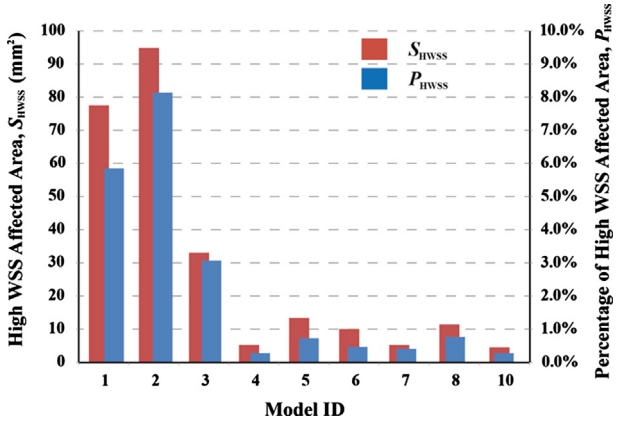

Fig. 10. High WSS influence on the studied stenosed carotid bifurcations.

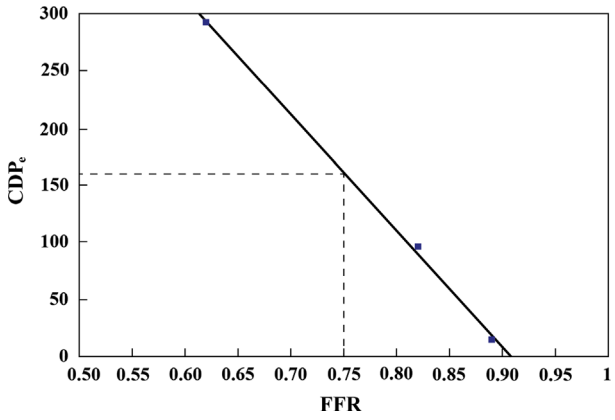

Fig. 11. Linear relation between CDP$_e$ and FFR.

3.4. *Computational efficiency assessment*

In order to evaluate the efficiency of the proposed modeling strategy for research or clinical use, the computational cost was monitored for each work stage (Fig. 12). The total time cost for a complete computational hemodynamics work of each single carotid bifurcation model was approximately around 19 h. The CFD simulation for each carotid bifurcation model was performed by a HP XW6600 workstation, 6 CPU (E5440 2.83 GHz) were assigned for local parallel run mode, and the total simulation time is around 10 h. The second most time consuming (4.3 hrs) work is geometry reconstruction, due to manual operation for segmentation of the geometry from MR images. Structured meshing (2.1 h) is also very

Table 3
Numerical simulation based CDP$_e$ and FFR values of the studied stenotic models.

ID	1	2	3	4	5	6	7	8	10
CDP$_e$	54.30	235.67	8.96	2.86	16.84	1.14	0.75	0.21	17.99
FFR (%)	85.54	67.69	90.00	90.61	89.23	90.78	90.82	90.87	89.12

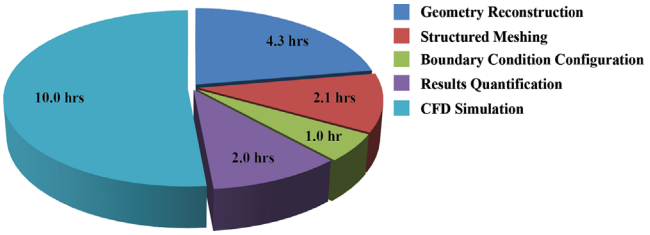

Fig. 12. Time cost summary for each work stage of the computational hemodynamics.

user-intensive as the block shape varies among individuals due to different branch curvatures and stenosis severities. The configuration of boundary conditions only cost 1 h, which is the shortest portion among all work stages. In order to extract and process the generated data, simulation results quantification took 2 h per patient-specific model.

Overall, the time cost by manual work involved in the CFD preparation and results analysis is 9.4 h for each carotid model. It is envisioned that the progression towards a more automated segmentation and meshing algorithm, the analysis stage could be reduced by half the time (e.g. 2 h). Furthermore where high fidelity accuracy is not needed, then an unstructured mesh which can be produced automatically would reduce the meshing time down to around 0.5 h. Therefore by optimizing the work flow the manual work for a single patient carotid artery could be as quick as 5hrs work. Furthermore with the use of high performance computing clusters, the CFD simulation time could be reduced right down to just one hour.

Some research assumptions of this work may restrict the accuracy of results. First, the influence of the vessel compliance is not taken into account, and this can be improved by implementing fluid structure interaction in the future. Another is the use of the representative inflow waveform. In clinical diagnosis, using Doppler ultrasound or phase-contrast MR imaging can measure the flow directly. However, these assumptions simplify the research when the time costs become important or even critical for the treating physician in practice. Therefore, on the basis of the time efficiency of the proposed numerical platform is highly dependent on computer hardware configuration and intensive user involvement, the total time for a computational hemodynamics platform to report its findings from MR scans, could be as quick as 6hrs turn-around which is highly feasible for clinical use. In addition, in some particular cases, if the vascular morphology is relatively maintained in healthy condition, and plaque burden analysis is not necessary, the overall time cost can be further shortened.

4. Conclusion

Image-based anatomical evaluations alone can approximately determine the artery stenosis burden, but cannot provide further detailed evidence to quantify the stenosis severity in addition to geometry occlusion measurement. In this paper, after the numerical accuracy was validated with published experimental results of two representative carotid bifurcations, a systematic methodology of high performance computational hemodynamics of atherosclerotic carotid bifurcation artery was proposed and performed on ten selected patient-specific realistic carotid bifurcation models. As TAWSS based analysis of the stenotic carotid bifurcation models can capture the abnormally high WSS lesion sites as well as the disturbed flow regions quantified by high OSI, therefore, the risk of direct endothelial injury and the consequent progression of plaque could be assessed and predicted. Based on the simulation results, it was found that the presence of plaque increases the WSS due to the accelerated blood flow, which can cause plaque erosion and thrombosis leading to stroke. Meanwhile, disturbed flow regions are established downstream of the stenosis lesion, where the endothelial cells are predisposed to dysfunction and atherogenesis. Eventually, the lesion-induced flow disturbances may contribute to a continuous stream-wise growth of the lesion over time.

In order to reveal the effects of the plaque existence on blood transportation performance, the pressure drop coefficient was introduced through adopting a linear relationship with fractional flow reserve, which further accesses the occlusion percentage of blood transportation based on the generated numerical simulation results. In addition, the influence of the presence of probe wire can also be prevented. Associating with the widely adopted clinical criteria, the severity of the stenosis can be easily stratified and modeled to proper treatment strategy. With necessary assumptions to simplify the research when the time costs become important or even critical for the treating physician in practice, the presented research applied with limitations can still provide evidential approaches to cardiovascular treatment in a quick time-frame. Although the current turn-around time cost for each stenotic model was 19 h, through optimization techniques within the work flow, this can be reduced down to 6 h which could prove to be of high clinical relevance.

Conflict of interest statement

The research work in this paper is original and has not been published anywhere. This work was performed independently by the authors and has no conflict of interest with third parties.

Acknowledgments

The authors acknowledge financial support provided by the Australian Research Council (ARC Project ID DP0986183), and Jingliang Dong also especially thanks for the scholarship provided by China Scholarship Council (CSC Student ID 2010608027) and RMIT University.

References

[1] S. al Rajeh, A. Awada, G. Niazi, E. Larbi, Stroke 24 (1993) 1635–1639.
[2] R. Ross, Nature 362 (1993) 801–809.
[3] European Carotid Surgery Trialists' (ECST) Collaboratvie Group, Lancet 337 (1991) 1235–1243.
[4] M. Taxon, Hemodynamic Basis of Atherosclerosis with Critique of the Cholesterol-Heart Disease Hypothesis, Begell House, Wallingford, U.K., 1995.
[5] S. Chien, Ann. Biomed. Eng. 36 (2008) 554–562.
[6] D. Tang, C. Yang, S. Mondal, F. Liu, G. Canton, T.S. Hatsukami, C. Yuan, J. Biomech. 41 (2008) 727–736.
[7] S.W. Lee, L. Antiga, J.D. Spence, D.A. Steinman, Stroke 39 (2008) 2341–2347.
[8] F.J. Gijsen, F.N. van de Vosse, J.D. Janssen, J. Biomech. 32 (1999) 601–608.
[9] C.M. Schirmer, A.M. Malek, J. Neurointerventional Surg. 4 (2012) 448–455.
[10] M. Tambasco, D.A. Steinman, Ann. Biomed. Eng. 31 (2003) 1054–1065.
[11] K.W. Lee, N.B. Wood, X.Y. Xu, Med. Eng. Phys. 26 (2004) 823–840.
[12] J.Y. Tu, K.K.L. Wong, S.C.P. Cheung, R. Beare, T. Phan, J. Med. Imaging Health Inf. 1 (2011) 116–125.
[13] K. Perktold, R.O. Peter, M. Resch, G. Langs, J. Biomech. Eng. 13 (1991) 507–515.
[14] Y. Fan, W. Jiang, Y. Zou, J. Li, J. Chen, X. Deng, Acta Mech. Sin. 25 (2009) 249–255.
[15] S.Z. Zhao, X.Y. Xu, M.W. Collins, A.V. Stanton, A.D. Hughes, S.A. Thom, Med. Eng. Phys. 21 (1999) 207–214.
[16] D.R. Wells, J.P. Archie Jr., C. Kleinstreuer, J. Vasc. Surg. 23 (1996) 667–678.
[17] C. Kleinstreuer, S. Hyun, J.R. Buchanan Jr., P.W. Longest, J.P. Archie Jr, G.A. Truskey, Crit. Rev. Biomed. Eng. 29 (2001) 1–64.
[18] J.F. LaDisa Jr., M. Bowers, L. Harmann, R. Prost, A.V. Doppalapudi, T. Mohyuddin, O. Zaidat, R.Q. Migrino, Med. Phys. 37 (2010) 784–792.
[19] N.A. Buchmann, Development of Particle Image Velocimetry for In-Vitro Studies of Arterial Haemodynamics, Ph.D. Thesis, Department of Mechanical Engineering, University of Canterbury, Christchurch, 2010.
[20] L.R. Sprouse, G.H. Meier, F.N. Parent, R.J. Demasi, C.J. Lesar, C. Nelms, K. Carter, M.J. Marcinczyk, R.G. Gayle, B. Mendoza, Vasc. Endovascular. Surg. 39 (2005) 143–151.

[21] D.W. Holdsworth, C.J.D. Norley, R. Frayne, D.A. Steinman, B.K. Rutt, Physiol. Meas. 20 (1999) 219–240.
[22] M. Zamir, The Physics of Pulsatile Flow, Springer-Verlag, Berlin, 2000.
[23] J.L. Dong, K.K.L. Wong, J.Y. Tu, Int. J. Numer. Methods Biomed. Eng. 29 (2013) 476–491.
[24] F.J. Gijsen, E. Allanic, F.N. van de Vosse, J.D. Janssen, J. Biomech. 32 (1999) 705–713.
[25] Z. Lou, W.J. Yang, J. Biomech. 26 (1993) 37–49.
[26] Y. Hoi, B.A. Wasserman, E.G. Lakatta, D.A. Steinman, J. Biomech. Eng. 132 (2010) 121008–121014.
[27] F. Ghalichi, X.Y. Deng, Biorheology 40 (2003) 637–654.
[28] S. Kefayati, T.L. Poepping, Med. Eng. Phys. 35 (2013) 898–909.
[29] D.L. Fry, Circ. Res. 22 (1968) 165–197.
[30] J.D. Hellums, Microvasc. Res. 13 (1977) 131–136.
[31] J.M. Ramstack, L. Zuckerman, L.F. Mockros, J. Biomech. 12 (1979) 113–125.
[32] S.D. Gertz, W.C. Roberts, Am. J. Cardiol. 66 (1990) 1368–1372.
[33] C.R. White, M. Haidekker, X. Bao, J.A. Frangos, Circulation 103 (2001) 2508–2513.
[34] M.D. Deshpande, D.P. Giddens, J. Fluid. Mech. 97 (1980) 65–89.
[35] B.B. Lieber, D.P. Giddens, J. Biomech. 23 (1990) 597–605.
[36] B.A. Younis, S.A. Berger, J. Biomech. Eng. 126 (2004) 578–584.
[37] D. Birchall, A. Zaman, J. Hacker, G. Davies, D. Mendelow, Eur. Radiol. 16 (2006) 1074–1083.
[38] F.R. Menter, R.B. Langtry, S.R. Likki, Y.B. Suzen, P.G. Huang, S. Völker, J. Turbomach. 128 (2006) 413–422.
[39] N.A. Buchmann, M. Yamamoto, M. Jermy, T. David, J. Biomech. Sci. Eng. 5 (2010) 421–435.
[40] D.N. Ku, D.P. Giddens, C.K. Zarins, S. Glagov, Arteriosclerosis 5 (1985) 293–302.
[41] C. Bertolotti, V. Deplano, J. Fuseri, P. Dupouy, J. Biomech. 34 (2001) 1049–1064.
[42] J.M. Zhang, L.P. Chua, D.N. Ghista, T.M. Zhou, Y.S. Tan, Med. Eng. Phys. 30 (2008) 226–247.
[43] P.F. Davies, Nat. Clin. Pract. Cardiovasc. Med. 6 (2009) 16–26.
[44] S.W. Lee, L. Antiga, D.A. Steinman, J. Biomech. Eng. 131 (2009) 0610131–0610137.
[45] C.J. Slager, J.J. Wentzel, F.J. Gijsen, A. Thury, A.C. van der Wal, J.A. Schaar P.W. Serruys, Nat. Clin. Pract. Cardiovasc. Med. 2 (2005) 456–464.
[46] J. Suo, J.N. Oshinski, D.P. Giddens, Mol. Cell. Biomech.: MCB 5 (2008) 9–18.
[47] G. García-Cardeña, J.I. Comander, B.R. Blackman, K.R. Anderson, M. A. Gimbrone, Ann. N. Y. Acad. Sci. 947 (2001) 1–6.
[48] N.H. Pijls, B. Van Gelder, P. Van der Voort, K. Peels, F.A. Bracke, H.J. Bonnier, M.I. el Gamal, Circulation 92 (1995) 3183–3193.
[49] K.L. Gould, Am. J. Physiol.: Heart Circ. Physiol. 291 (2006) H2583–H2585.
[50] S.A. Chamuleau, M. Siebes, M. Meuwissen, K.T. Koch, A.E. Spaan, J.J. Piek, Am. J. Physiol.—Heart Circ. Physiol. 285 (2003) H2194–H2200.
[51] J.A. Spaan, J.J. Piek, J.I. Hoffman, M. Siebes, Circulation 113 (2006) 446–455.
[52] E. Rajabi-Jaghargh, K.K. Kolli, L.H. Back, R.K. Banerjee, Biomed. Eng. Online 10 (2011) 51.
[53] R.K. Banerjee, K.D. Ashtekar, T.A. Helmy, M.A. Effat, L.H. Back, S.F. Khoury, Biomed. Eng. Online 7 (2008) 1–22.